

Single-Image Lens Flare Removal

Yicheng Wu^{1*} Qiurui He² Tianfan Xue² Rahul Garg² Jiawen Chen²
 Ashok Veeraraghavan¹ Jonathan T. Barron²

¹Rice University ²Google Research

{yicheng.wu, vashok}@rice.edu {qiurui, tianfan, rahulgarg, jiawen, barron}@google.com

Abstract

Lens flare is a common artifact in photographs occurring when the camera is pointed at a strong light source. It is caused by either multiple reflections within the lens or scattering due to scratches or dust on the lens, and may appear in a wide variety of patterns: halos, streaks, color bleeding, haze, etc. The diversity in its appearance makes flare removal extremely challenging. Existing software methods make strong assumptions about the artifacts' geometry or brightness, and thus only handle a small subset of flares. We take a principled approach to explicitly model the optical causes of flare, which leads to a novel semi-synthetic pipeline for generating flare-corrupted images from both empirical and wave-optics-simulated lens flares. Using the semi-synthetic data generated by this pipeline, we build a neural network to remove lens flare. Experiments show that our model generalizes well to real lens flares captured by different devices, and outperforms start-of-the-art methods by 3dB in PSNR.

1. Introduction

Photographs of a scene that contains a strong light source often exhibit lens flare — a salient visual artifact caused by unintended reflections and scattering within the camera. Flare artifacts can be distracting, reduce detail, and may completely occlude image content. Despite significant efforts by manufacturers to design optics that minimize lens flare, when bright, even small light sources can produce substantial flare artifacts when imaged using modern consumer cameras.

Flare patterns in images depend on the optics of the lens, light source location, manufacturing imperfections, and scratches and dust accumulated through everyday use. The diversity in the underlying cause of lens flare leads to diversity in its presentation. As Fig. 1 shows, typical flares



Figure 1. Lens flare artifacts frequently occur in photographs with strong light sources. They exhibit a wide range of shapes, colors, and locations, and are difficult to remove with existing methods.

may include halos, streaks, bright lines, spokes, saturated blobs, color bleeding, ringing, rainbow streaks, and many others. This diversity makes the problem of flare removal exceedingly challenging.

Most existing methods for lens flare removal [1, 4, 25] do not account for the physics of flare formation, but rather naïvely rely on template matching or intensity thresholding to identify the presence of flare. As such, they can only detect and potentially remove limited types of flares, such as bright spots, and do not work well in more complex real-world scenarios. Our goal is to directly model the real-world diversity and complexity of flare presentations and develop an algorithm for single-image flare removal that does not require any hardware modification. It is therefore applicable to flare-corrupted images already acquired using conventional cameras.

1.1. Challenges, key ideas, and contributions

Physically-realistic model for flare Unlike existing approaches, we present a physically-realistic yet practically-tractable model for lens flare. We make the key observation that lens flare is an additive layer on top of the underlying image, and that it is induced by either scattering or internal reflection. For the scattering effects of scratches, dust, and other defects, we create an elegant wave optics model

*This work was done while Yicheng was an intern at Google.

that is shown to be accurate in reality. For the unintended reflections between lens elements, we take a rigorous data-driven approach as a full mathematical characterization is impractical.

Flare dataset Collecting a large number of perfectly-aligned image pairs with and without lens flare would be tedious at best and impossible at worst: the camera and the scene would need to be static (a particularly difficult requirement given that most lens flare occurs outdoors and involve the sun), and one would need some mechanism for “switching” the artifacts on and off without also changing the illumination of the scene. With significant effort this can be accomplished by collecting pairs of images taken on a tripod where in one image the photographer manually places an occluder between the illuminant and the camera. But this approach is too labor-intensive to produce the thousands or millions of image pairs usually required to train a neural network. Furthermore, this approach only works when the flare-causing illuminant lies outside of the camera’s field of view (see Fig. 7), which limits its utility. To overcome this data collection challenge, we exploit the physically-realistic model and build a novel pipeline to generate a large and diverse dataset of *semi-synthetic* flare-corrupted images along with ground-truth flare-free images.

Learning-based flare removal We propose a learning-based technique for flare removal, where we utilize the large, diverse dataset to train a convolutional neural network. At test time, our method requires only a single RGB image taken with a standard camera and is able to remove different types of flare across a variety of scenes. Although our model is trained on semi-synthetic data only, it performs well on real (non-synthetic) images. To the best of our knowledge, this is the first general-purpose method for removing lens flare from a single image.

2. Related work

Existing solutions for flare removal can be categorized into (a) hardware solutions intended to mitigate the presence of flare in the optics, (b) software-only methods that attempt post-capture image enhancement, and (c) hardware–software solutions that capture additional information.

Hardware solutions The lenses of high-end cameras often employ sophisticated optical designs and materials to reduce flare. As each glass element is added to a compound lens to improve image quality, there is also an increased probability that light is reflected from its surface to create flare. One widely used technique is to apply anti-reflective (AR) coating to lens elements, which reduces internal reflection by destructive interference. However, the thickness of this coating can only be optimized for certain wavelengths and angles of incidence and therefore cannot

be perfect. Additionally, adding an AR coating to all optical surfaces is expensive, and may preclude or interfere with other coatings (e.g., anti-scratch and anti-fingerprint).

Computational methods Many post-processing techniques have been proposed to remove flare. Deconvolution has been used to remove flare in X-ray imaging [8, 22] or HDR photography [20]. These approaches depend critically on the assumption that the point spread function of the flare does not vary spatially, which is generally not true. Other solutions [1, 4, 25] adopt a two-stage process: detecting lens flare based on their unique shape or intensity (i.e., by identifying a saturated region), and then recovering the scene behind the flare region using inpainting [6]. These solutions only work on limited types of flare (e.g., flare spots), and are vulnerable to the misclassification of all bright regions as flare. Additionally, these techniques classify each pixel as either “flare” or “not flare”, ignoring the fact that most lens flares are better modeled as a semitransparent layer on top of the underlying scene.

Hardware–software co-design Researchers have used computational imaging for flare removal, where camera hardware and post-processing algorithms are designed in conjunction. Talvala et al. [24] and Raskar et al. [19] attempt to selectively block flare-causing light using structured occlusion masks and recover the flare-free scene using either direct–indirect separation or a light-field-based algorithm. Though elegant, they require special hardware and are therefore limited in their practicality.

Learning-based image decomposition While no learning-based techniques exist for flare removal, they have been developed for other artifact removal applications such as reflection removal [7, 16, 28], dehazing [3], rain removal [18, 26], and denoising [2]. These methods attempt to decompose an image into “clean” and “corrupt” by training a neural network. Their success relies heavily on high-quality domain-specific training datasets, which this work tries to address for the first time.

3. Physics of lens flare

An ideal camera, when in focus, is supposed to refract and converge all rays from a point light source to a single point on the sensor. In practice, real lenses scatter and reflect light along unintended paths, resulting in flare artifacts [13], as shown in Fig. 2(a). For each incident light ray, the scattered and reflected rays only constitute a small fraction. So although flare is omnipresent, it is imperceptible in most photographs. But, when a strong light source is many orders of magnitude brighter than the rest of the scene (e.g., the sun), the small fraction of scattered and reflected rays from this bright light will lead to visible artifacts in other pixels on the image. The geometry of the scattering from

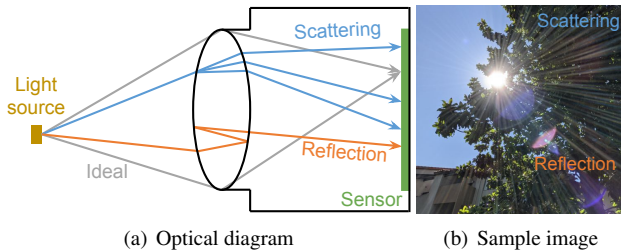


Figure 2. Cameras are intended to focus light from a point source at exactly one point on the sensor (gray rays). However, dust and scratches may cause scattering (blur rays), leading to haze and bright streaks “emitting” radially from the light source. Additionally, internal reflections (orange rays) can occur between the optical surfaces of lens elements (only one element is shown), resulting in disk- or arc-shaped bright spots. This reflective flare may also have a color tint, as the anti-reflective coating only blocks certain wavelengths.

dust and scratches, and that of the multiple reflections, introduce the characteristic visual patterns of flare. At a high level, flare can be classified into two principal categories: scattering-induced and reflection-induced.

Scattering flare While ideal lenses are 100% refractive, real lenses have many imperfections that cause light to scatter when it interacts with the lens surfaces. The scattering (or diffraction) could be due to manufacturing defects (dents or other sharp surface discontinuities), or due to normal wear (e.g., dust and scratches). As a consequence, apart from the primary rays that are refracted, a secondary set of rays are scattered or diffracted instead of following their intended paths. While dust adds a rainbow-like effect, scratches introduce streaks that appear to “emit” radially from the light source. Scattering may also reduce contrast in the region around the light source, leading to a hazy appearance.

Reflective flare In a practical lens system, each air–glass interface poses an opportunity for a small amount of reflection (typically about 4%). After an even number of reflections, the rays may hit the sensor at an unintended location, forming a reflection pattern. Even if we assume the light is reflected exactly twice, for a lens module containing n optical elements ($n \approx 5$ for a modern camera), there are $2n$ optical surfaces, and thus $n(2n - 1)$ potential flare-causing combinations. On the image, these reflective flares typically lie on a straight line joining the light source and the principal point. They are sensitive to the light source’s angle of incidence, as demonstrated by Fig. 4(b), but not to rotation about the optical axis. The flare’s shape depends on the aperture’s geometry, and its size on the location of the reflective surfaces. For cameras with small apertures (e.g., smartphones), the reflection may be partially blocked by the aperture more than once, resulting in arc-shaped ar-

tifacts. As mentioned in Sec. 2, AR coating may be used to reduce reflection — typically reducing reflections at the air–glass interface to below 1%. However, the effectiveness of this coating also depends on the wavelength, so lens flare may exhibit a variety of color tints (often blue, purple, or pink). It is important to note that reflective flare depends on lens design, and therefore cameras that have the same lens design (e.g., all iPhone 12 main camera modules) are expected to produce similar reflective flares when imaging the same scene.

Challenges in flare removal The different types of flares are often difficult to visibly distinguish or separate. The appearance of the observed flare may vary significantly based on the properties of the light source (e.g., location, size, intensity, and spectrum), and of the lens (e.g., design and defects). For these reasons, it is impractical to build a completely physics-based algorithm to analytically identify and remove each type of flare, especially when multiple artifacts are present in the same image. Moreover, such algorithms, even if built, will likely not generalize to different cameras. Therefore, we suggest a data-driven approach.

4. Model for lens flare

Unlike many vision problems in a supervised setting, it is hard to obtain a dataset of flare-corrupted and flare-free image pairs. As a result, we build a physically-realistic, semi-synthetic model.

The additive nature of light implies we can model flare as an additive artifact on top of the “ideal” image — the reduction in the intensity of the “ideal” rays is negligible. We will first explain how the scattering and reflective flares can be modeled and generated, and then use them to synthesize flare-corrupted and flare-free image pairs.

4.1. Scattering flare

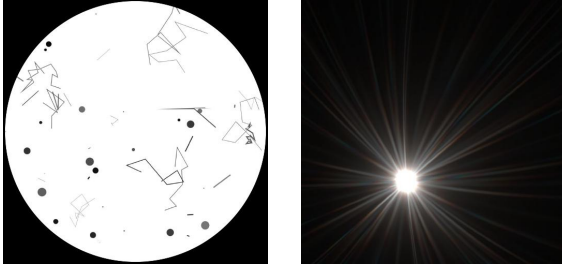
Formulation Under the thin-lens approximation, an optical imaging system can be characterized by the complex-valued *pupil function* $P(u, v)$: a 2D field describing, for each point (u, v) on the aperture plane, the lens’s effect on the amplitude and phase of an incident wave with wavelength λ :

$$P_\lambda(u, v) = A(u, v) \cdot \exp(i\phi_\lambda(u, v)). \quad (1)$$

Here, A is an *aperture function*, a property of the optics that represents its attenuation of the incident wave’s amplitude.¹ In its simplest form, a camera with an aperture of a finite radius r has an aperture function of

$$A(u, v) = \begin{cases} 1 & \text{if } u^2 + v^2 < r^2 \\ 0 & \text{otherwise} \end{cases}. \quad (2)$$

¹Strictly speaking, lens optics can also introduce a phase shift, in which case A becomes a complex-valued function. However, this has shown little difference in our simulation results, so we assume A is real-valued.



(a) Aperture of a dirty lens (b) Simulated flare

Figure 3. To simulate a scattering flare component, we generate a number of apertures (a) with random dots and lines that resemble defects. Wave optics then allows us to compute the image (b) of one light source imaged by that synthetic aperture.

ϕ_λ in Eq. 1 describes the phase shift, which depends on the wavelength as well as the 3D location of the light source (x, y, z) . Omitting the aperture coordinates (u, v) , ϕ_λ can be written as:

$$\phi_\lambda(x, y, z) = \phi_\lambda^S(x/z, y/z) + \phi_\lambda^{DF}(z) \quad (3)$$

where the linear term ϕ^S is determined by the angle of incidence, and the defocus term ϕ^{DF} depends on the depth z of the point light source. Once fully specified, the pupil function P in Eq. 1 can be used to calculate the PSF by a Fourier transform [9]:

$$PSF_\lambda = |\mathcal{F}\{P_\lambda\}|^2 \quad (4)$$

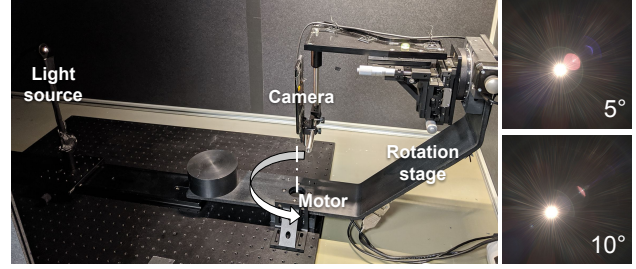
which, by definition, is the image of a point light source at (x, y, z) formed by a camera with aperture function A . This is the flare image that we desire.

Sampling PSFs To mimic dust and scratches on the lens, we add dots and streaks of random size and transparency to the simple aperture function A in Eq. 2. An example synthetic aperture produced by our procedure is shown in Fig. 3(a), and details are included in the supplement. We generate a total of 125 different apertures.

For a given point light source at location (x, y, z) with a single wavelength λ , the two terms in the phase shift formula in Eq. 3 can be computed deterministically. The PSF for this light source, PSF_λ , can thus be determined by substituting A and ϕ_λ into Eq. 4.

To simulate a light source across the full visible spectrum, we sample PSF_λ for all wavelengths λ from 380nm to 740nm with an interval of 5nm, resulting in a 73-vector at each pixel of the PSF. The full-spectrum PSF is then left-multiplied by a spectral response function SRF (a 3×73 matrix) to derive the PSF measured by the RGB sensor:

$$\begin{bmatrix} PSF_R(s, t) \\ PSF_G(s, t) \\ PSF_B(s, t) \end{bmatrix} = SRF \begin{bmatrix} PSF_{\lambda=380\text{nm}}(s, t) \\ \dots \\ PSF_{\lambda=740\text{nm}}(s, t) \end{bmatrix} \quad (5)$$



(a) Capture setup (b) Real flare

Figure 4. We capture images of real lens flare using a strong light source in a dark room. The camera is mounted on a motorized rotation stage that reproduces a wide range of incident angles. Sample images captured at different angles are shown in 4(b).

where (s, t) are the image coordinates. This produces a flare image for a light source located at (x, y, z) .

To construct our dataset of scattering flares, we randomly sample the aperture function A , the light source’s 3D location (x, y, z) , and the spectral response function SRF . Details can be found in the supplement. We further apply optical distortion (e.g., barrel and pincushion) to augment the PSF_{RGB} images. One example of final output is shown in Fig. 3(b). We generate a total of 2,000 such images.

4.2. Reflective flare

The reflective flare component is difficult to simulate via rendering techniques [11, 15], as they require a complete and accurate characterization of the optics, which is often unavailable. However, lenses of similar design share similar internal reflection paths, so data collected from one instance of the camera often generalize well to other similar devices.

We capture images of reflective flare in a laboratory setting consisting of a bright light source, a programmable rotation stage, and a fixed-aperture smartphone camera with a $f = 13\text{mm}$ lens (35mm equivalent), as shown in Fig. 4(a). The setup is insulated from ambient light during capture.

The camera is rotated programmatically so that the light source traces (and extends beyond) the diagonal field of view, from -75° to 75° . We capture one HDR image every 0.15° , resulting in 1,000 samples. Adjacent captures are then interpolated by 2x using the frame interpolation algorithm of [17], giving us 2,000 images. During training, images are further augmented by random rotation, as reflective flare is rotationally symmetric about the optical axis.

4.3. Synthesizing flare-corrupted images

A flare-corrupted image I_F is generated by adding a flare-only image F to a flare-free natural image I_0 in linear space (pre-tonemapping raw space where pixel intensities are additive), as illustrated in Fig. 5. We also add random Gaussian noise whose variance is sampled once per image

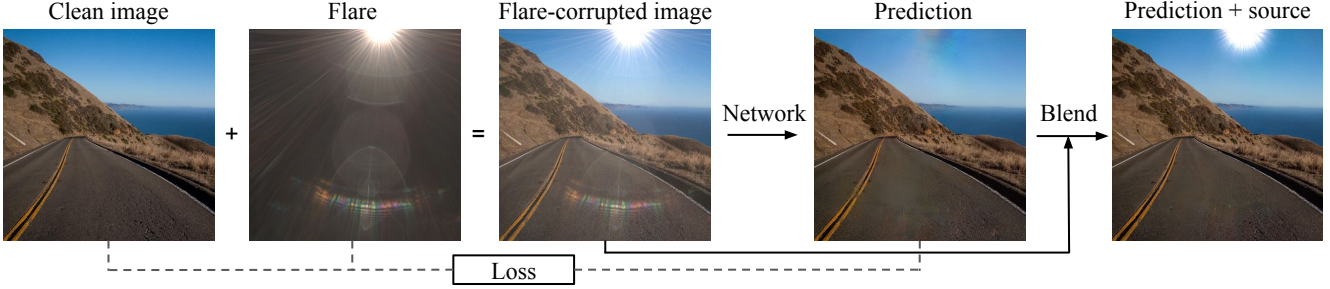


Figure 5. Our approach consists of three steps: 1) We generate training input by randomly compositing a flare-free natural image and a flare image. 2) A convolutional neural network is trained to recover the flare-free scene (in which the light source may also have been removed, which is undesirable). 3) After prediction, we blend the input light source back into the output image.

from a scaled chi-square distribution $\sigma^2 \sim 0.01\chi^2$:

$$I_F = I_0 + F + N(0, \sigma^2). \quad (6)$$

The flare-free image I_0 is sampled from the 24k Flickr images in [28], and is augmented by random flips and brightness adjustments. Since the Flickr images are already gamma-encoded, we approximately linearize them by applying an inverse gamma curve where γ is sampled uniformly from [1.8, 2.2] to account for the fact that its exact value is unknown.

The flare-only image F is sampled from both captured and simulated datasets. We show they both are necessary in an ablation study in Sec. 6.2. Random affine transformation (e.g., scaling, translation, rotation, and shear) and random white balance are applied for additional augmentation. Randomization details are in the supplement.

5. Reconstruction algorithm

Given a flare-corrupted image $I_F \in [0, 1]^{M \times N \times 3}$, our goal is to design a neural network $f(I_F, \Theta)$ to predict flare-free images I_0 , where Θ are the network weights. We use the U-Net architecture [21] as it provides dense pixel-wise prediction. Details about the network architecture and the training process can be found in the supplement. During training, the input and output image size is $512 \times 512 \times 3$.

5.1. Losses

Our goal is to remove *only* the flare caused by a bright light source. But the flare-only images F in our datasets contain *both* the flare and the light source, as it is impractical to physically separate the two during capture or simulation. If we trained the network naïvely, it would attempt to hallucinate the image without the light source, which is not the intended use of this model and also a waste of model capacity. Therefore, to prevent the model from inpainting the scene behind the light source, we ignore the saturated pixels when computing the loss, assuming they are due to the light source. Note that in general, saturated pixels are unrecoverable and contain almost no information about the scene.

Specifically, we modify the raw network output $f(I_F, \Theta)$ with a binary saturation mask M before computing losses. The mask M corresponds to the pixels where the luminance of input I_F is greater than a threshold (0.99 in our experiments). For pixels inside M , we replace it with the ground truth I_0 so that the loss is zero for such regions²:

$$\hat{I}_0 = I_0 \odot M + f(I_F, \Theta) \odot (1 - M), \quad (7)$$

where \odot denotes element-wise multiplication.

During training, we minimize the sum of two losses: an image loss and a *flare loss*:

$$\mathcal{L} = \mathcal{L}_I + \mathcal{L}_F. \quad (8)$$

The image loss \mathcal{L}_I encourages the predicted flare-free image \hat{I}_0 to be close to the ground truth I_0 both photometrically and perceptually. The data term is an L1 loss on the RGB values between \hat{I}_0 and I_0 . The perceptual term is computed by feeding \hat{I}_0 and I_0 through a pre-trained VGG-19 network [23]. Like [28], we penalize the absolute difference between $\Phi_\ell(\hat{I}_0)$ and $\Phi_\ell(I_0)$ at selected feature layers `conv1_2`, `conv2_2`, `conv3_2`, `conv4_2`, and `conv5_2`. To sum up, the image loss can be expressed as:

$$\mathcal{L}_I = \left\| \hat{I}_0 - I_0 \right\|_1 + \sum_{\ell} \lambda_{\ell} \left\| \Phi_{\ell}(\hat{I}_0) - \Phi_{\ell}(I_0) \right\|_1. \quad (9)$$

The flare loss \mathcal{L}_F encourages the predicted flare to be similar to the ground-truth flare F , which proves useful in reducing the artifacts in the predicted flare-free image (Sec. 6.2). Here, the predicted flare \hat{F} is calculated as the difference between the network input and the masked network output:

$$\hat{F} = I_F - f(I_F, \Theta) \odot (1 - M). \quad (10)$$

Similarly, \mathcal{L}_F also has a data term and a perceptual term:

$$\mathcal{L}_F = \left\| \hat{F} - F \right\|_1 + \sum_{\ell} \lambda_{\ell} \left\| \Phi_{\ell}(\hat{F}) - \Phi_{\ell}(F) \right\|_1. \quad (11)$$

²We replace rather than exclude masked pixels because the perceptual loss in Eq. 9 requires a complete image.

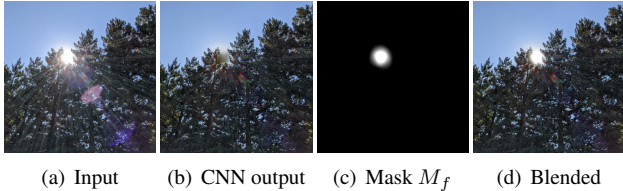


Figure 6. We deliberately prevent our network from learning to inpaint the saturated regions (illuminants), so its output (b) is undefined in these regions. To preserve highlights, we compute a mask (c) for the saturated regions of the input. The masked area in the network output is then replaced by the input pixels, producing a more realistic final result (d) in which the flare is removed, but not the illuminant that produced it.

5.2. Post-processing for light source blending

The losses explicitly prevent the network from “learning to inpaint” anything in the saturated regions, so its output there can be arbitrary. In practice, it tends to remove the light source so that it is more similar to the surrounding pixels, as shown in Fig. 6(b). Since the goal of this work is to remove the flare, and not the light source, we post-process the network output to add back the light source.

A key observation is that the flare-causing light source is very likely saturated in the input image (otherwise it would not result in a visible flare). Hence, it can be identified easily based on intensity. To create a gradual transition, we feather the mask M defined in Sec. 5.1 at its boundary to construct M_f . Details and parameters are in the supplement. With this we blend the input image and output image using the feathered mask in linear space:

$$I_B = I_F \odot M_f + f(I_F, \Theta) \odot (1 - M_f). \quad (12)$$

An example output image is shown in Fig. 6(d).

6. Results

To evaluate how our model trained on semi-synthetic data generalizes, we use three types of test data: 1) synthetic images with ground truth (Sec. 4), 2) real images without ground truth, and 3) real images with ground truth. To obtain 3), we capture a pair of images on a tripod with a strong illuminant just outside the field of view. In one image, strong flare-causing rays can still enter the lens, producing flare artifacts. In the other image, a small out-of-view occluder (e.g., a lens hood) is carefully placed between the illuminant and the camera, blocking the flare-causing rays.

6.1. Comparison with prior work

Because there is no prior work on learning-based flare removal, we compare our results against several non-learned flare spot removal algorithms [4, 1]. We also evaluate existing solutions for related image decomposition tasks: dehazing [10], reflection removal [28, 16], and rain removal [18].

Our method shows superior quantitative performance on both synthetic and real data, as shown in Table 1. To remove the influence of the light source when computing metrics, the masked region is replaced by the ground truth following Eq. 7. Fig. 7 shows a few visual comparisons with PSNR and SSIM for each image.

We also conduct a user study with 20 participants where we present each user with a real-world image with lens flare, alongside two predicted flare-free images: one from our method and the other from one of the 4 baselines. We then ask the user to identify which of the two outputs better removes the lens flare. We use 75 images from 3 different sets: images captured by the same type of lens as was used in Sec. 4.2, images captured by five other lenses with different focal lengths, and images taken from [4]. To avoid bias, we shuffle the images for each instance of the study. As Table 2 shows, our method outperforms all others by a significant margin on all 3 datasets. Unsurprisingly, it performs slightly worse when tested on the lenses that are different from our training set. Note that users prefer our method to the method of Chabert [4] on their dataset (85% vs. 15%).

6.2. Ablation study

In this section, we study two key components in our model to demonstrate their impact on the output.

Flare loss Since most flares are brighter than the underlying scene, we need to ensure that the network does not simply learn to darken all bright regions. We explicitly model

Method	Synthetic		Real	
	PSNR	SSIM	PSNR	SSIM
Input image	21.13	0.843	18.57	0.787
Flare spot removal [4]	21.01	0.840	18.53	0.782
Flare spot removal [1]	21.13	0.843	18.57	0.787
Raindrop removal [18]	19.61	0.754	19.01	0.779
Dehaze [10]	12.55	0.680	12.35	0.573
Dereflection [28]	20.71	0.767	22.28	0.822
Dereflection [16]	21.72	0.837	21.02	0.805
Ours	30.37	0.944	25.55	0.850

Table 1. Quantitative comparison against related methods on synthetic and real data.

Comparison	Dataset 1	Dataset 2	Dataset 3
Ours : Flare spot removal [4]	98%: 2%	97%: 3%	85%:15%
Ours : Raindrop removal [18]	94%: 6%	90%:10%	80%:20%
Ours : Dereflection [28]	83%:17%	78%:22%	64%:36%
Ours : Dereflection [16]	89%:11%	82%:18%	84%:16%
Average	91%: 9%	87%:13%	78%:22%

Table 2. Percentages of images where the users favor our results vs. prior work. Test data come from three datasets. Dataset 1 is captured by the same lens design as in Sec. 4.2. Dataset 2 is captured by five other lens types with different focal lengths. Dataset 3 contains images from [4]. We outperform existing methods in most of the cases, even on Chabert’s own dataset.

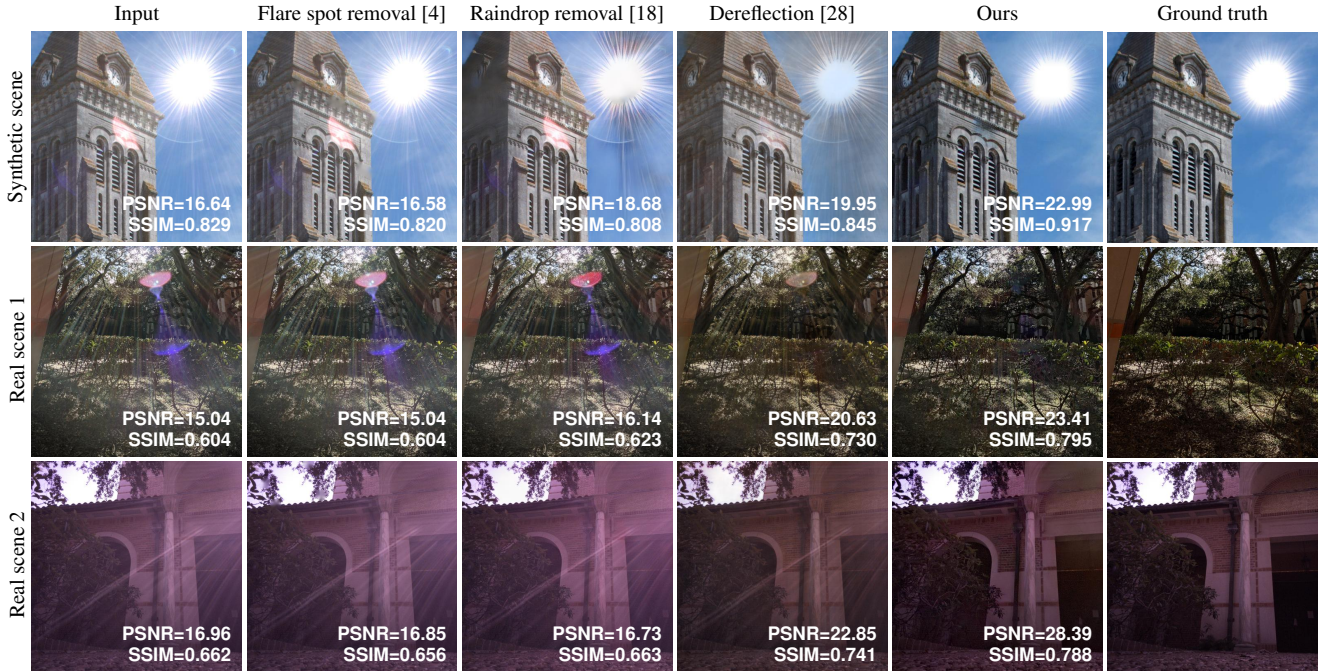


Figure 7. Visual comparison between three related methods and ours, evaluated on both synthetic and real scenes. Our method removes lens flare more accurately and produces cleaner outputs.



Figure 8. Our method robustly removes lens flare of various shapes, colors, and locations on diverse real-world images. It generalizes reasonably to multiple light sources (column 2). When there is no significant flare (last column), the input is kept intact.

this in our flare loss \mathcal{L}_F (Eq. 11). In Fig. 9, we show test set results from the models trained with and without \mathcal{L}_F . Without \mathcal{L}_F , the network tends to reduce the intensity for bright regions even if they are not part of the flare.

Captured and simulated flare data We claimed in Sec. 4 that the captured data mostly account for reflective flare, whereas the simulated data covers the scattering case. To show that both components are necessary, we train two ablated models, each with one of the data sources excluded. As expected, models trained with flare-only images taken from the captured or simulated dataset alone underperform the model trained with both datasets, as shown in Fig. 10.

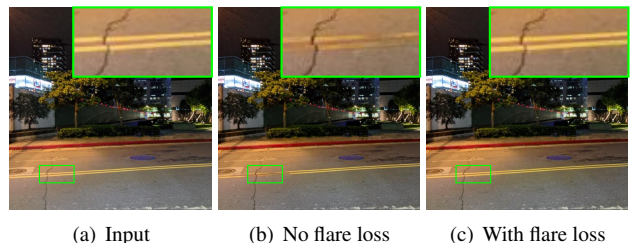


Figure 9. Without our flare loss \mathcal{L}_F , bright regions in the input (a) are incorrectly removed, especially for images taken at night (b). \mathcal{L}_F makes the model more robust against such errors (c).

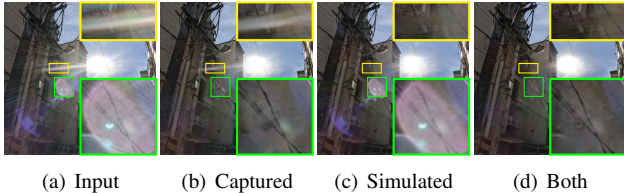


Figure 10. The model trained with captured flare only (b) (containing mostly reflective and limited scattering flare) is less effective at removing streak-like scattering artifacts, whereas the simulation-only model (c) is unable to remove reflective flare patterns. Training with both datasets (d) produces superior results.

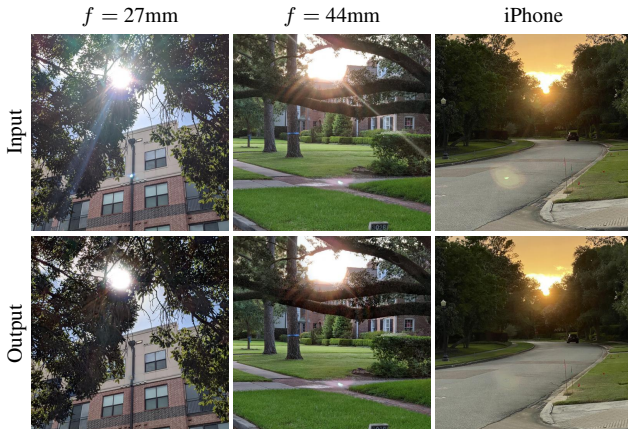
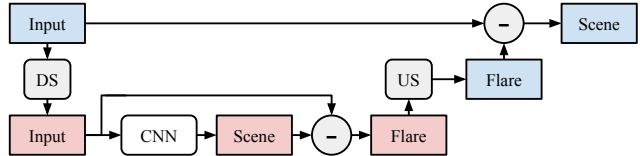


Figure 11. Although our model has only seen real flare patterns from the ultra wide-angle camera of an Android smartphone ($f = 13\text{mm}$), it can generalize effectively to the phone’s other lenses ($f = 27$ and 44mm), as well as another smartphone camera (iPhone).

6.3. Generalization

Across scenes As our semi-synthetic dataset contains diverse flare patterns and scenes, the trained model generalizes well across a wide variety of scene types. As shown in Fig. 8, the input images contain flares with different shapes, colors, and locations, and scenes with varying subjects and lighting conditions. The model produces a high-quality output in most scenarios. When there is no flare in the input image, the network correctly performs a no-op.

Across cameras As mentioned in Sec. 4.2, all of our reflective flare training images come from one smartphone camera with focal length $f = 13\text{mm}$. We also test our model on different camera designs excluded from training. As shown in Fig. 11, the model is still able to reduce lens flare effectively, echoing the findings of the user study in Table 2. This indicates that our approach can potentially be used for a broad range of cameras.



(a) Pipeline: blue and red blocks represent high- and low-res respectively.



Figure 12. Because lens flares are mostly low-frequency, our algorithm can be trivially extended to high-resolution inputs. As shown in (a), we downsample (DS) a high-resolution input (b), predict a flare-free image (c) with our network (CNN), and compute the flare as the difference. This predicted flare is then upsampled (US) to high resolution, and subtracted from the input image to produce a high-resolution flare-free scene (d).

6.4. High-resolution images

Our network is trained using 512×512 images. The naïve way to apply our method to a higher-resolution input is to train at the desired resolution (e.g., 2048×2048), which requires 16x more bandwidth at both training and test time.

Fortunately, we can leverage the fact that lens flare is predominantly a low-frequency artifact. To apply our model to a high-resolution image, we can bilinearly downsample the input image, predict a reduced-resolution flare-only image, bilinearly upsample it back to full resolution, and subtract it from the original input (see Fig. 12). This allows a network trained at a fixed low resolution to process high-resolution images without significant quality loss. In our test on an Intel Xeon E5 CPU, the processing time for a 2048×2048 input is reduced from 8s to 0.55s when performing the inference at 512×512 .

7. Conclusion

We have introduced a novel, tractable, and physically-realistic model for lens flare. By building a semi-synthetic data generation pipeline using this principled image formation model, we are able to train a convolutional neural network to recover a clean flare-free image from a single flare-corrupted image without the need for real training data. Our method is shown to achieve accurate results across a range of scenes and cameras. To our knowledge, this is the first general-purpose lens flare removal technique.

A. Simulating random scattering flare

To synthesize scattering flare using our wave optics model, we randomly sample the aperture function A , the light source’s 3D location (x, y, z) , and the spectral response function SRF .

Notations

- $N(\mu, \sigma^2)$: normal distribution with mean μ and standard deviation σ .
- $U(a, b)$: uniform distribution on the interval $[a, b]$.
- k_λ : the wavenumber corresponding to wavelength λ . Can be computed as $k_\lambda = 2\pi/\lambda$.

A.1. Aperture function

As Fig. 3(a) of the main text illustrates, we simulate dust and scratches with random dots and polylines on a clean disk-shaped aperture of radius $R = 3000$ pixels.

For each aperture function, we randomly generate $n_d \sim N(30, 5^2)$ dots with maximum radius $r_d^{\max} \sim N(100, 50^2)$. Each individual dot’s radius r_d is drawn independently from $U(0, r_d^{\max})$.

Additionally, we also generate $n_p \sim N(30, 5^2)$ polylines, each of which consists of a random number (1 – 16) of line segments connected from end to end. The maximum segment length for each aperture function is $l_p^{\max} \sim N(20, 5^2)$, and each individual line segment’s length is drawn independently from $U(0, l_p^{\max})$.

The opacity of each of the dots and polylines is sampled independently from $U(0, 1)$, and its location (u, v) on the aperture plane is also drawn uniformly.

A.2. Phase shift

The light source’s 3D location (x, y, z) determines the phase shift ϕ_λ of the pupil function P_λ . As shown in Eq. 3 of the main text, it consists of a linear term ϕ_λ^S and a defocus term ϕ_λ^{DF} .

The linear phase shift ϕ_λ^S on the aperture plane becomes a spatial shift on the sensor plane due to the Fourier transform $\mathcal{F}\{\cdot\}$ in Eq. 4 of the main text. For an 800×800 sensor image with the center as the origin, the center of the light source (x, y) is sampled from $U(-500, 500)$.

The term $\phi_\lambda^{DF}(z)$ is the defocus aberration due to the mismatch between the in-focus depth z_0 of the lens and the actual depth z of the light source. The analytical expression for $\phi_\lambda^{DF}(z)$ is:

$$\begin{aligned} \phi_\lambda^{DF}(z) &= k_\lambda \frac{u^2 + v^2}{2} \left(\frac{1}{z} - \frac{1}{z_0} \right) \\ &= k_\lambda \cdot r(u, v)^2 \cdot W_m(z) \end{aligned} \quad (13)$$

where k_λ is the wavenumber, (u, v) are aperture coordinates, and $r(u, v) = \sqrt{u^2 + v^2}/R$ is the relative displace-

ment on the aperture plane. $W_m(z)$ is defined as:

$$W_m(z) = \frac{R^2}{2} \left(\frac{1}{z} - \frac{1}{z_0} \right) \quad (14)$$

and quantifies the amount of defocus in terms of the depth z . Since we do not target any specific camera device (i.e., specific R and z_0 values), it suffices to sample the value of W_m directly, in our case from $N(0, \sigma^2)$. We use $\sigma = 5/k_{\lambda=550\text{nm}}$.

A.3. Spectral response function

The spectral response $SRF_c(\lambda)$ describes the sensitivity of color channel c to wavelength λ , where $c \in \{\text{R}, \text{G}, \text{B}\}$.

We model $SRF_c(\lambda)$ as a Gaussian probability density function $N(\mu_c, \sigma_c^2)$. The mean μ_c is the central wavelength of each channel in nanometers, and is drawn from $\mu_R \sim U(620, 640)$, $\mu_G \sim U(540, 560)$, and $\mu_B \sim U(460, 480)$. The standard deviation σ_c represents the width of the pass-band of each color channel, and is drawn independently for each channel from $U(50, 60)$.

We then discretize the wavelength λ in $SRF_c(\lambda)$ for each of the RGB channels at 5nm intervals from $\lambda = 380\text{nm}$ to 740nm , resulting in a 73-vector for each channel. The 3 vectors are stacked to produce an instance of SRF in the form of a 3×73 matrix.

B. Flare-only image augmentation

We augment the captured flare-only images F by applying random geometric and color transformations. For geometric augmentation, we generate a 3×3 affine transformation matrix with random rotation ($\sim U(0, 2\pi)$), random translation ($\sim U(-10, 10)$ pixels), random shear angle ($\sim U(-\pi/9, \pi/9)$), and random scale ($\sim U(0.9, 1.2)$ for x and y independently). For color augmentation, we multiply each color channel with a random weight in $U(0, 10)$. Color channels are only clipped after combining the augmented flare-only image with the clean image.

C. Network details

C.1. U-Net architecture

The input image I_F is $512 \times 512 \times 3$. Each convolution operator consists of a 3×3 convolution and ReLU activation. We use 2×2 max pooling for downsampling and resize-convolution for upsampling. Concatenation is applied between the encoder and decoder to avoid the vanishing gradient problem. At the final layer, we use a sigmoid function to squeeze the activations to the $[0, 1]$ range.

C.2. Training details

We train for 1.2 million iterations (approximately 60 epochs over the 20 thousand images in the Flickr dataset

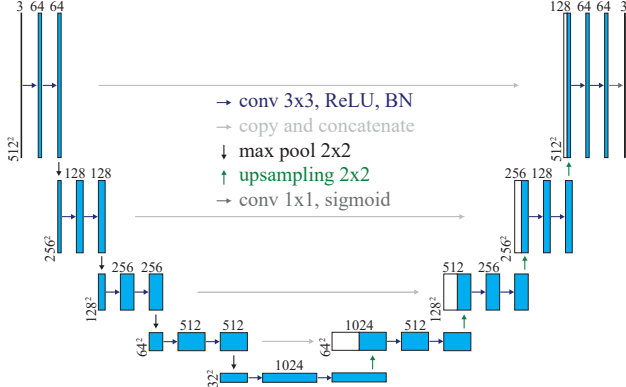


Figure 13. The U-Net architecture we used in the flare removal task.

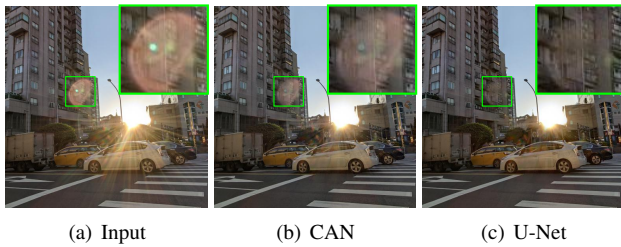


Figure 14. Compared to the context aggregation network (CAN) [27], U-Net is able to produce cleaner output with less residual flare.

using on-the-fly data augmentation) with batch size 2 on an Nvidia V100 GPU. We use the Adam optimizer [12] with its default parameters and a fixed learning rate of 10^{-4} .

C.3. Context Aggregation Network

For comparison, we also trained a context aggregation network (CAN) [27], a popular architecture for tasks such as reflection removal, on our dataset. CAN first extracts features from a pre-trained VGG-19 network [23], then passes them through eight 3×3 dilated convolution layers. As shown in Fig. 14, U-Net is able to remove more flare and produce cleaner output. One possible explanation is that U-Net simply has more model capacity since it has roughly $10\times$ the number of trainable parameters.

D. Mask feathering

As mentioned in Sec. 5.2 of the main text, we detect the light source and create a feathered mask M_f to smoothly blend the bright illuminants into our network output.

Starting from a binary mask M (the pixels where the input luminance is greater than 0.99), we apply morphological opening with a disk kernel of size equal to 0.5% of the image size. To find the primary light source, we partition the mask into connected components and find the equivalent diameter D of the largest region (the diameter of a circle with

the same area as the region). We blur the binary mask M using a disk kernel of diameter D . Finally, we scale the blurred mask intensity by 3 guarantee that all the pixels inside the light source are saturated after blurring, and clip the mask to $[0, 1]$. This is our M_f used in Eq. 12 which has a gradual transition.

E. Flare removal for downstream tasks

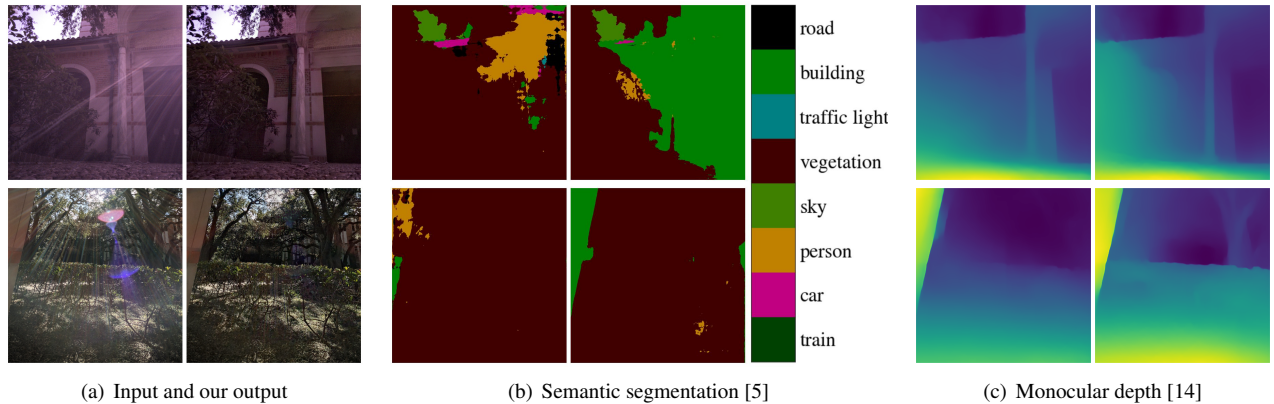
In Fig. 15, we show that removing lens flare may benefit downstream tasks such as semantic segmentation and depth estimation. We look forward to thoroughly investigating the effect flare removal on a range of computer vision algorithms.

F. More results

Fig. 16 provides more visual comparisons between our method and prior work. Overall, we have 20 real test images with ground truth.

We also show 24 additional test images captured using the same type of lens as in Sec. 4.2 of the main text (Fig. 17), and 24 test images captured using 7 other lens types with different focal lengths (Fig. 18).

Although our flare removal algorithm works for various flare types, there is still room for improvement. In challenging scenes with strong flare and/or substantial noise (e.g., captured at night), our method cannot remove the flare completely. In addition, bright regions (e.g., clouds) are sometimes treated as flare and incorrectly darkened.



(a) Input and our output

(b) Semantic segmentation [5]

(c) Monocular depth [14]

Figure 15. A pair of images with flare and our output (a). Semantic segmentation (b) results are improved once flare is removed using our method. Similarly, monocular depth estimation (c) is also more accurate, e.g., the depth of the bush on the left in the top image and the depth of the tree in the distance in the lower image.

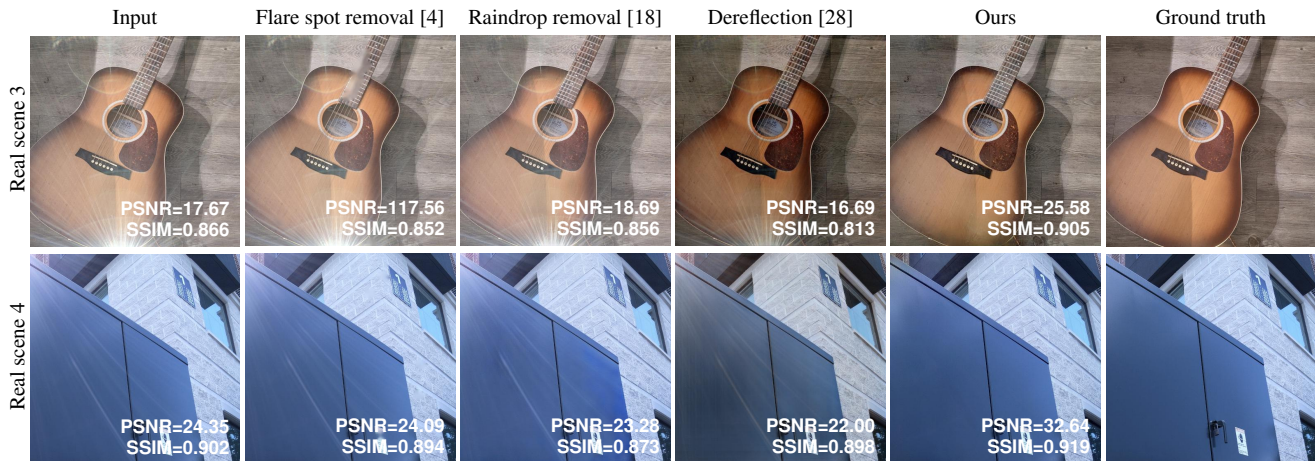


Figure 16. More visual comparison between three related methods and ours on real scenes, with PSNR and SSIM values.

References

- [1] CS Asha, Sooraj Kumar Bhat, Deepa Nayak, and Chaithra Bhat. Auto removal of bright spot from images captured against flashing light source. *IEEE DISCOVER*, 2019.
- [2] Tim Brooks, Ben Mildenhall, Tianfan Xue, Jiawen Chen, Dillon Sharlet, and Jonathan T Barron. Unprocessing images for learned raw denoising. *CVPR*, 2019.
- [3] Bolun Cai, Xiangmin Xu, Kui Jia, Chunmei Qing, and Dacheng Tao. Dehazenet: An end-to-end system for single image haze removal. *IEEE TIP*, 2016.
- [4] Floris Chabert. Automated lens flare removal. Technical report, Department of Electrical Engineering, Stanford University, 2015.
- [5] Liang-Chieh Chen, Yukun Zhu, George Papandreou, Florian Schroff, and Hartwig Adam. Encoder-decoder with atrous separable convolution for semantic image segmentation. *ECCV*, 2018.
- [6] Antonio Criminisi, Patrick Pérez, and Kentaro Toyama. Region filling and object removal by exemplar-based image inpainting. *IEEE TIP*, 2004.
- [7] Qingnan Fan, Jiaolong Yang, Gang Hua, Baoquan Chen, and David Wipf. A generic deep architecture for single image reflection removal and image smoothing. *ICCV*, 2017.
- [8] K Faulkner, CJ Kotre, and M Louka. Veiling glare deconvolution of images produced by x-ray image intensifiers. *International Conference on Image Processing and its Applications*, 1989.
- [9] Joseph W Goodman. *Introduction to Fourier optics*. Roberts and Company Publishers, 2005.
- [10] Kaiming He, Jian Sun, and Xiaoou Tang. Single image haze removal using dark channel prior. *IEEE TPAMI*, 2010.
- [11] Matthias Hullin, Elmar Eisemann, Hans-Peter Seidel, and Sungkil Lee. Physically-based real-time lens flare rendering. *SIGGRAPH*, 2011.
- [12] Diederik P Kingma and Jimmy Ba. Adam: A method for stochastic optimization. *arXiv:1412.6980*, 2017.
- [13] Rudolf Kingslake. *Optics in photography*. SPIE press, 1992.
- [14] Katrin Lasinger, René Ranftl, Konrad Schindler, and Vladlen Koltun. Towards robust monocular depth estimation: Mixing datasets for zero-shot cross-dataset transfer. *TPAMI*, 2020.

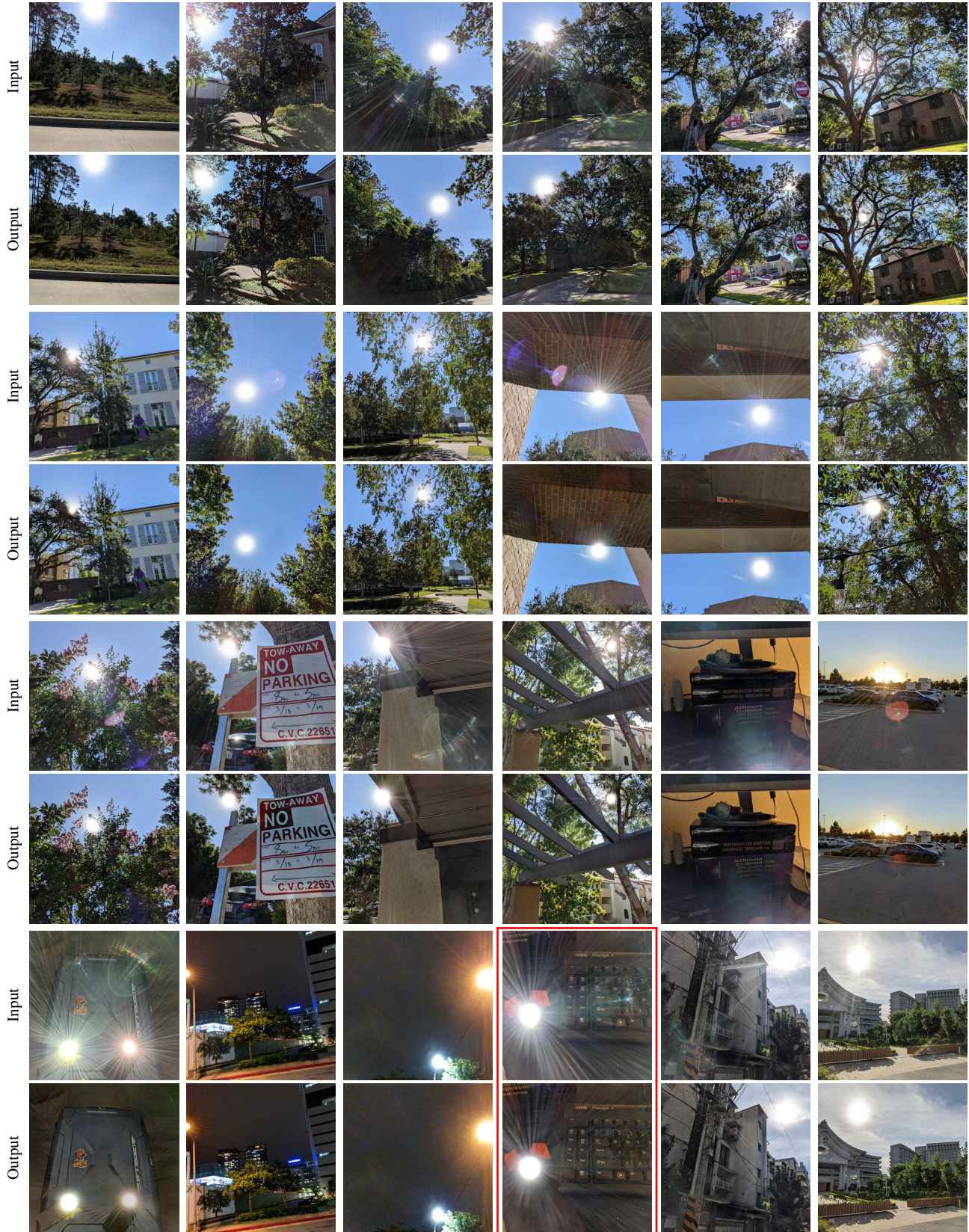


Figure 17. 24 testing images captured by the same type of lens as in Sec. 4.2 of the main text. While our method is effective in removing most of the lens flare, there are occasional failures where a noticeable portion of the flare is not removed (red box).

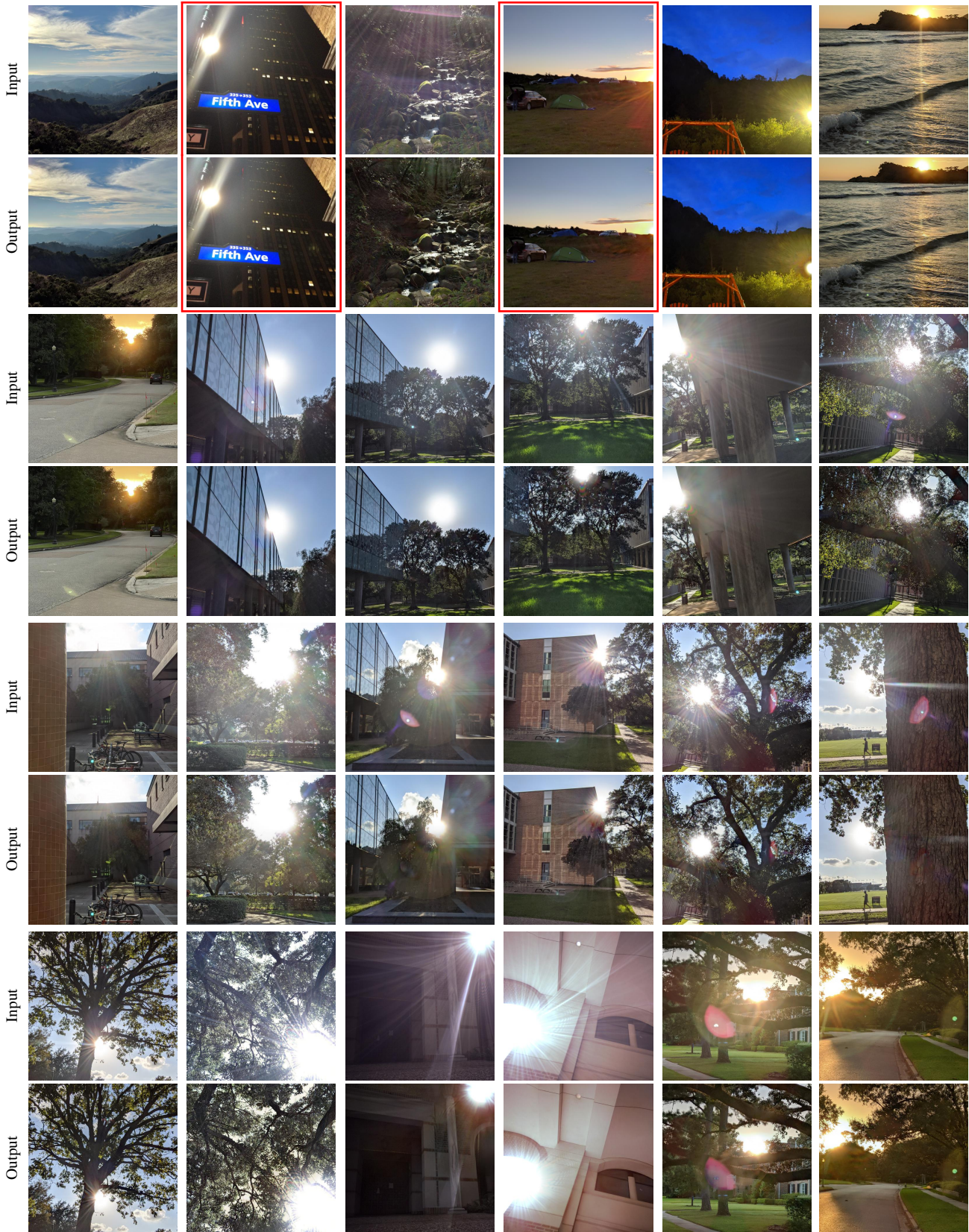


Figure 18. 24 testing images captured by 7 other lens types with different designs and focal lengths. Our method may sometimes fail to identify and remove the lens flare (first red box). Occasionally, it may also attempt to remove non-flare highlights, such as some of the clouds in the second red box.

- [15] Sungkil Lee and Elmar Eisemann. Practical real-time lens-flare rendering. *Computer Graphics Forum*, 2013.
- [16] Chao Li, Yixiao Yang, Kun He, Stephen Lin, and John E Hopcroft. Single image reflection removal through cascaded refinement. *CVPR*, 2020.
- [17] Simon Niklaus and Feng Liu. Context-aware synthesis for video frame interpolation. *CVPR*, 2018.
- [18] Rui Qian, Robby T Tan, Wenhan Yang, Jiajun Su, and Jiaying Liu. Attentive generative adversarial network for rain-drop removal from a single image. *CVPR*, 2018.
- [19] Ramesh Raskar, Amit Agrawal, Cyrus A Wilson, and Ashok Veeraraghavan. Glare aware photography: 4d ray sampling for reducing glare effects of camera lenses. *SIGGRAPH*, 2008.
- [20] Erik Reinhard, Wolfgang Heidrich, Paul Debevec, Sumanta Pattanaik, Greg Ward, and Karol Myszkowski. *High dynamic range imaging: acquisition, display, and image-based lighting*. Morgan Kaufmann, 2010.
- [21] Olaf Ronneberger, Philipp Fischer, and Thomas Brox. U-net: Convolutional networks for biomedical image segmentation. *MICCAI*, 2015.
- [22] J Anthony Seibert, O Nalcioglu, and W Roeck. Removal of image intensifier veiling glare by mathematical deconvolution techniques. *Medical physics*, 1985.
- [23] Karen Simonyan and Andrew Zisserman. Very deep convolutional networks for large-scale image recognition. *ICLR*, 2015.
- [24] Eino-Ville Talvala, Andrew Adams, Mark Horowitz, and Marc Levoy. Veiling glare in high dynamic range imaging. *ACM TOG*, 2007.
- [25] Patricia Vitoria and Coloma Ballester. Automatic flare spot artifact detection and removal in photographs. *Journal of Mathematical Imaging and Vision*, 2019.
- [26] Wei Wei, Deyu Meng, Qian Zhao, Zongben Xu, and Ying Wu. Semi-supervised transfer learning for image rain removal. *CVPR*, 2019.
- [27] Fisher Yu and Vladlen Koltun. Multi-scale context aggregation by dilated convolutions. *ICLR*, 2016.
- [28] Xuaner Zhang, Ren Ng, and Qifeng Chen. Single image reflection separation with perceptual losses. *CVPR*, 2018.